Universal Rim Thickness in Unsteady Sheet Fragmentation

Y. Wang, R. Dandekar, N. Bustos, S. Poulain, and L. Bourouiba*
The Fluid Dynamics of Disease Transmission Laboratory, Massachusetts Institute of Technology, Cambridge, Massachusetts 02139, USA

(Received 13 January 2018; published 16 May 2018)

Unsteady fragmentation of a fluid bulk into droplets is important for epidemiology as it governs the transport of pathogens from sneezes and coughs, or from contaminated crops in agriculture. It is also ubiquitous in industrial processes such as paint, coating, and combustion. Unsteady fragmentation is distinct from steady fragmentation on which most theoretical efforts have been focused thus far. We address this gap by studying a canonical unsteady fragmentation process: the breakup from a drop impact on a finite surface where the drop fluid is transferred to a free expanding sheet of time-varying properties and bounded by a rim of time-varying thickness. The continuous rim destabilization selects the final spray droplets, yet this process remains poorly understood. We combine theory with advanced image analysis to study the unsteady rim destabilization. We show that, at all times, the rim thickness is governed by a local instantaneous Bond number equal to unity, defined with the *instantaneous*, *local*, unsteady rim acceleration. This criterion is found to be robust and universal for a family of unsteady inviscid fluid sheet fragmentation phenomena, from impacts of drops on various surface geometries to impacts on films. We discuss under which viscous and viscoelastic conditions the criterion continues to govern the unsteady rim thickness.

DOI: 10.1103/PhysRevLett.120.204503

Unsteady fluid fragmentation is ubiquitous and important for a wide range of industrial processes [1,2], health applications [3–6], or pathogen dispersal in agriculture [7]. Fluid fragmentation generates numerous droplets that can travel over large distances and disperse their biological and chemical payloads. Prior work focused on characterizing the droplet size distribution as a function of the breakup geometry and fluid properties [2,8,9]. Theoretical insights focused on steady fragmentation, such as Savart sheets [9–11]. However, an important class of fragmentation processes are in fact *unsteady*: they continuously shed droplets with time-varying properties.

Unsteady sheet fragmentation occurs for crown splash upon drop impact on a thin liquid film [12–15] or deep pool [16,17], or crescent-moon splash upon drop-drop interactions on surfaces [7,18,19]. These situations generate an expanding sheet of time-varying velocity and thickness profiles, bounded by a rim of time-varying thickness which destabilizes into droplets. The rim is the critical link between the sheet and droplets. While linear instabilities of rims were extensively discussed [14,20,21], time-resolved observations and theoretical insights on unsteady rim destabilization are lacking. Here, we present the first systematic demonstrations on the role of unsteadiness in rim destabilization.

Prior work on the canonical unsteady fragmentation process from drop impact on a surface of comparable size [Fig. 2(a)] [21–27] assumed that most droplets are shed after full radial sheet expansion. Our recent work, however, shows that the droplet size and speed distributions are determined during the sheet expansion [28], in which the *rim destabilization* plays a key role. Unsteadiness introduces a more subtle dynamics than the classic debated dichotomy between Rayleigh-Plateau [29–31] and Rayleigh-Taylor instabilities [21,32,33]. A prior study [34] considered the interplay between the coupled Rayleigh-Plateau and Rayleigh-Taylor instability using linear stability analysis. Here we consider them jointly acting on an inviscid cylindrical liquid jet subject to an acceleration as shown in Fig. 1 (inset). The dispersion relation of the coupled instability can be derived as (see Supplemental Material [35])

$$\omega^2 = \frac{1}{2}\left(-\chi(k) + \sqrt{\chi(k)^2 - 4\psi(k)}\right),$$
$$\text{with} \quad \chi(k) = \frac{kI_1(k)}{I_0(k)}(k^2-1) + \frac{kI_2(k)}{I_1(k)}k^2$$
$$\text{and} \quad \psi(k) = \frac{k^2 I_2(k)}{2I_0(k)}[2(k^2-1)k^2 - (\mathrm{Bo}/4)^2], \quad (1)$$

where $I_n(k)$ is the first kind of modified Bessel function of order n, k is the wave number nondimensionalized by the rim radius $b/2$, and ω is the growth rate nondimensionalized by the rim capillary time scale $\tau_c = \sqrt{\rho b^3/8\sigma}$, where ρ and σ are the density and surface tension of the fluid, respectively. $\mathrm{Bo} = \rho(-\ddot{R})b^2/\sigma$ is the *instantaneous* and *local* rim Bond number based on the *instantaneous* rim thickness b and acceleration $\ddot{R}$. When $\mathrm{Bo} = 0$, (1) simplifies to $\omega^2 = [kI_1(k)/I_0(k)](k^2-1)$, the inviscid Rayleigh-Plateau instability dispersion relation. This

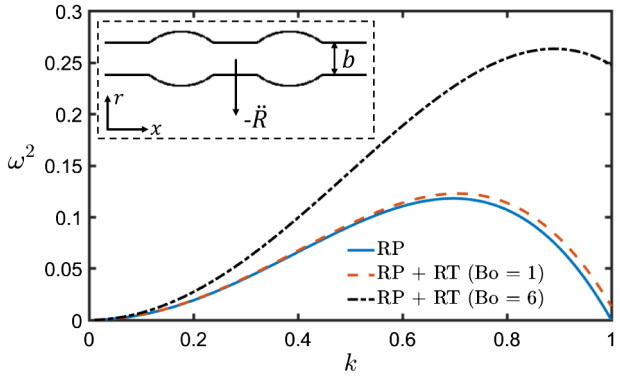

FIG. 1. Dimensionless dispersion relation of the coupled Rayleigh-Plateau (RP) and Rayleigh-Taylor (RT) instabilities for different Bond number Bo compared to that of the Rayleigh-Plateau instability. Inset: fluid cylinder of diameter b subject to an acceleration $-\ddot{R}$.

remains true at first order for Bo $\sim O(1)$ (Fig. 1). Only for Bo $\gg 1$ does the dispersion relation deviate significantly from that of Rayleigh-Plateau, yet remaining distinct from that of the Rayleigh-Taylor instability of a planar sheet $\omega^2 = k(\mathrm{Bo} - k^2)$.

The unsteadiness of the acceleration $-\ddot{R}$ aggravates the complexity of the rim destabilization. To gain key physical insights on its role, we developed advanced image-processing algorithms that capture the contour of the rim-ligament system, and separated the rim from the ligaments [Fig. 2(a)] to measure precisely the time-varying rim thickness b. Figure 2(b) shows that the rim thickness b matches very well with the time-varying capillary length $l_c = \sqrt{\sigma/\rho(-\ddot{R})}$ based on the *instantaneous* sheet acceleration $-\ddot{R}$, i.e., $b = l_c$. This leads to an important criterion: the *instantaneous, local* Bond number of the rim Bo $= \rho b^2(-\ddot{R})/\sigma = 1$ holds at all times. Moreover, such criterion is independent of the impact Weber number We $= \rho u_0^2 d_0/\sigma$, where u_0 is the impacting velocity of the drop and d_0 its diameter [Fig. 2(b) inset].

To rationalize the Bo $= 1$ criterion we first examine the force balance on a growing corrugation on the rim [Fig. 2(a) lower inset]. Distinct from a free liquid jet, the rim of an unsteady expanding sheet does not fragment into droplets directly. Corrugations grow along the rim to form ligaments while fluid continuously enters the rim from the sheet at a time-varying rate. As a small corrugation grows to form a bulge of size proportional to the rim thickness b, in the noninertial reference frame of the rim, the deceleration exerts a fictitious force on the bulge, pulling it away from the rim. Simultaneously, surface tension pulls the bulge toward the rim [Fig. 2(a) inset]. The resulting force balance on the bulge is

$$m_b(-\ddot{R}) \sim \sigma b \Rightarrow b \sim \sqrt{\frac{\sigma}{\rho(-\ddot{R})}}, \tag{2}$$

where $m_b \sim \rho b^3$ is the mass of the bulge. Thus, if the rim thickness is much larger than the local instantaneous capillary length, a bulge is pulled away from the rim.

We can compute the prefactor of the scaling law (2) combining the linear instability analysis discussed earlier with the local momentum conservation of the growing bulge. When Bo$\sim O(1)$ the modified dispersion relation (1) is close to that of the inviscid Rayleigh-Plateau instability (Fig. 1). The associated fastest growing wavelength is $\lambda_{\max} = 2\pi/k_{\max} \simeq 4.5b$. Considering a spherical bulge of volume equal to that contained within one wavelength of the fluid column with diameter $d_b = (27/4)^{1/3} b \simeq 1.9b$,

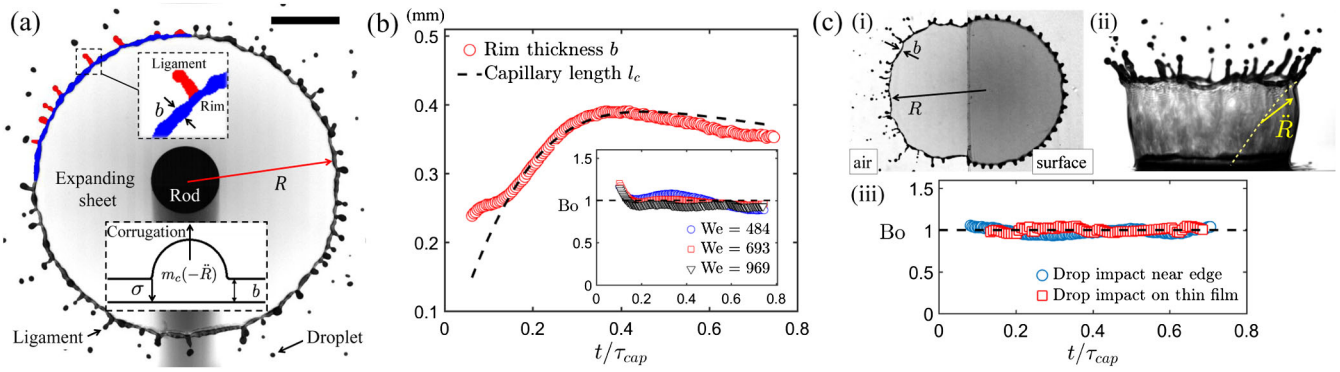

FIG. 2. (a) Unsteady sheet fragmentation upon drop impact on a target of comparable size which ensures a horizontal expanding sheet [22]. Scale bar is 6 mm. Upper inset: rim-ligament separation by our image processing algorithm. Lower inset: schematic diagram of a local corrugation. (b) Time evolution of the sheet rim thickness compared to the local instantaneous capillary length l_c based on the rim acceleration $-\ddot{R}$ for We $= 693$. Time is nondimensionalized by the global capillary time $\tau_{\mathrm{cap}} = \sqrt{\rho d_0^3/8\sigma}$ of sheet expansion, where d_0 is the diameter of the impacting drop. Inset: local, instantaneous Bond number of the rim Bo $= 1$, robust for three different Weber numbers. (c) Sheet fragmentation from (i) impact near a surface edge, causing the sheet's left part to expand in the air, and (ii) drop impact on a thin liquid film with a crown rising upward. (iii) Criterion of Bo $= 1$ holds for the rim in the air in case (i) and for the crown rim in case (ii).

and mass $m_b = \rho\pi d_b^3/6$, surface tension pulls on such bulge with a force $F_\sigma = \sigma\pi d_b$. The dimensionless growth rate of the fastest growing mode of the inviscid Rayleigh-Plateau instability is $\omega_{\max} = 0.343$ (Fig. 1). Thus, the characteristic growth timescale of a corrugation into a bulge is $\tau_g = \tau_c/\omega_{\max}$. Using the bulge radius $d_b/2$ as a characteristic length scale, the resulting growth speed is $v_b = d_b/2\tau_g$. Momentum conservation on the bulge reads

$$m_b(-\ddot{R}) + \rho A_b v_b^2 = \sigma\pi d_b, \tag{3}$$

where $A_b = \pi d_b^2/4$ is the bulge cross-section area, giving

$$b \simeq \sqrt{\frac{\sigma}{\rho(-\ddot{R})}} \Rightarrow \mathrm{Bo} = \frac{\rho(-\ddot{R})b^2}{\sigma} \simeq 1. \tag{4}$$

This result matches our data very well [Fig. 2(b)]. Besides sheet fragmentation upon drop impact on a surface of size comparable to the drop, we also show that the criterion $\mathrm{Bo} = 1$ applies to other fragmentation processes including asymmetric sheet expansion in the air from a drop impact near the edge of a surface [Fig. 2(c-i)] and for drop impacts on thin films leading to a crown [Fig. 2(c-ii)]. Despite changes in geometry and two-to-three dimensional sheet expansions, the unsteady local criterion $\mathrm{Bo} = 1$ regulating the rim thickness holds. This means that the local unsteady rim thickness retains the value of the *local and instantaneous* capillary length throughout the unsteady sheet expansion. This remains true as long as sufficient fluid enters the rim and viscous stresses are negligible as discussed hereafter.

The criterion of instantaneous local $\mathrm{Bo} = 1$ governing the unsteady rim thickness also applies to the fragmentation of fluids with a range of viscous and elastic properties summarized in Table 1 (see Supplemental Material [35]). Figure 3(b) shows the time evolution of the local instantaneous Bond number of the sheet rim for the same Weber of impact but different viscosity ν and elastic relaxation time τ_E. The $\mathrm{Bo} = 1$ criterion continues to hold within critical regions of viscous and elastic effects [Figs. 3(b) and 3(c)]. To better understand the effects of viscosity and elasticity, we examine the local rim Reynolds $\tilde{\mathrm{Re}} = v_b b/\nu$ in the noninertial rim frame (competition of inertial to viscous effects) and Deborah numbers $\tilde{\mathrm{De}} = \tau_E/\tau_g$ (competition of elastic to capillary effects). Using the characteristic velocity $v_b \simeq \sqrt{\sigma/\rho b}$ and time $\tau_g \simeq \sqrt{\rho b^3/\sigma}$ of rim destabilization, $\tilde{\mathrm{Re}} = \sqrt{\sigma b/\rho\nu^2}$ and $\tilde{\mathrm{De}} = \tau_E/\sqrt{\rho b^3/\sigma}$.

Prior studies of drop impacts gave a maximum radius of the expanding sheet $R_{\max} \sim \sqrt{\mathrm{We}} d_0$. Thus, the sheet deceleration scales as $(-\ddot{R}) \sim R_{\max}/\tau_{\mathrm{cap}}^2 \sim u_0/\tau_{\mathrm{cap}}$, where $\tau_{\mathrm{cap}} = \sqrt{\rho d_0^3/8\sigma}$ is the global capillary timescale characteristic of the sheet expansion. Experiments show that the variation in sheet deceleration during sheet expansion remains small compared to its mean value $\langle -\ddot{R}\rangle \simeq 2u_0/\tau_{\mathrm{cap}}$ (Fig. 2 in the Supplemental Material [35]). Substituting this expression into (4) gives $b \simeq 0.2\mathrm{We}^{-1/4} d_0$. Thus, the local Reynolds and Deborah numbers become

$$\tilde{\mathrm{Re}} \simeq 0.2\,\mathrm{Oh}^{-5/4}\,\mathrm{Re}^{-1/4} \quad \text{and} \quad \tilde{\mathrm{De}} \simeq 4\,\mathrm{De}\,\mathrm{We}^{3/8}, \tag{5}$$

where the Reynolds $\mathrm{Re} = u_0 d_0/\nu$, Ohnesorge $\mathrm{Oh} = \sqrt{\rho\nu^2/(\sigma d_0)}$, and Deborah numbers $\mathrm{De} = \tau_E/\tau_{\mathrm{cap}}$ are based on impact conditions. A regime map in terms of $\tilde{\mathrm{Re}}$ and $\tilde{\mathrm{De}}$ defined in (5) is shown in Fig. 3(c): circles show experiments for which $\mathrm{Bo} = 1$ holds and squares those for which it fails. The region within which $\mathrm{Bo} = 1$ holds is bounded by $\tilde{\mathrm{Re}} \gtrsim 8$ and $\tilde{\mathrm{De}} \lesssim 16$.

The dispersion relation $\omega = \omega(k)$ of the Rayleigh-Plateau instability used for the derivation of $\mathrm{Bo} = 1$ only

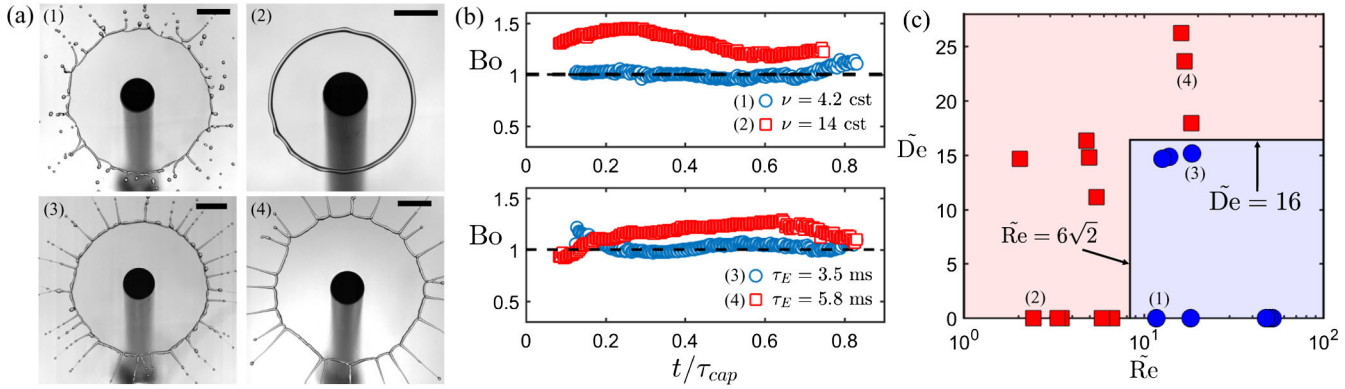

FIG. 3. (a) Sheet expansion upon drop impact on pole for fluids of different viscosity and elasticity. Scale bars are 6 mm. (b) Time evolution of the local instantaneous rim Bond number for the fluids shown in (a). (c) Regime diagram in terms of the local Reynolds number $\tilde{\mathrm{Re}}$ and Deborah number $\tilde{\mathrm{De}}$ defined in (5). Circles represent the experimental conditions for which $\mathrm{Bo} = 1$ holds, and squares the conditions for which it fails, for the rim of unsteady expanding sheet upon drop impact on a small surface. The criterion to determine if $\mathrm{Bo} = 1$ holds is that $0.8 < \langle \mathrm{Bo}\rangle < 1.2$.

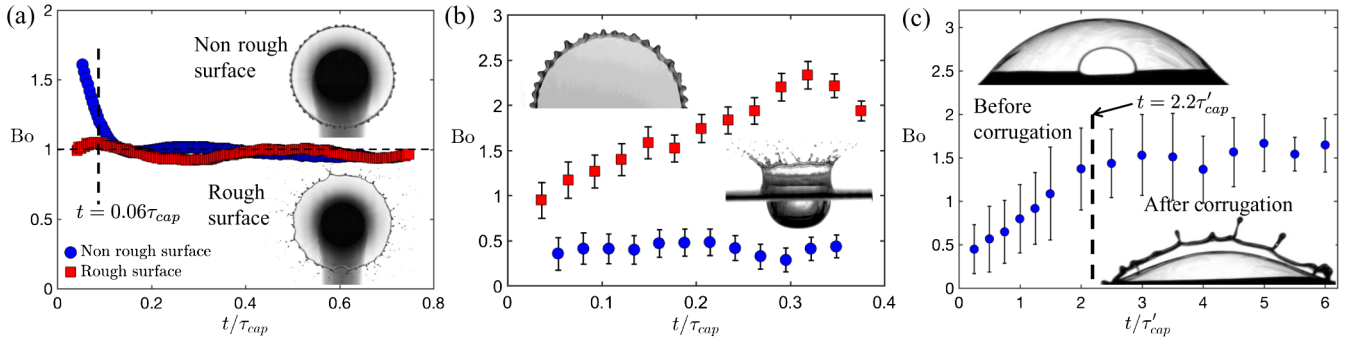

FIG. 4. (a) Time evolution of the local Bond number of the rim upon drop impact on a small smooth surface, compared with that upon impact on a rough surface for We = 693. The insets show the sheet at time $t = 0.06\tau_{\mathrm{cap}}$, when the fragmentation is occurring on the rough surface while it has not yet started on the smooth one. (b) Time evolution of the local Bond number of the rim from drop impact on a deep pool for We = 824 (circles) and from impact on a solid surface for We = 543 (squares), showing that Bo = 1 fails in these two cases. (c) Time evolution of the local Bond number of the rim from bubble bursting. The capillary time in this case is $\tau'_{\mathrm{cap}} = \sqrt{\rho(rh)^{3/2}/\sigma}$ with $r = 5.6$ mm and $h = 7.4$ μm the bubble cap radius and thickness, respectively. The Bond number is computed based on the centripetal acceleration measured at the early stage of the hole retraction on the bubble cap.

applies for inviscid fluids. The full relation accounting for both inertia and viscosity is implicit [36] but can be simplified asymptotically for small viscosity to yield the fastest-growing wave number $k^2_{\mathrm{max}} = 1/(2 + 6\sqrt{2}/\tilde{\mathrm{Re}})$ [37]. This shows that the inviscid dispersion relation no longer applies for $\tilde{\mathrm{Re}} < 6\sqrt{2}$. Thus, the Bo = 1 criterion should also fail when $\tilde{\mathrm{Re}} < 6\sqrt{2} \approx 8.5$, which matches our experimental data very well [Fig. 3(c)].

Prior studies on the Rayleigh-Plateau instability [38–42] showed that the breakup of a column of fluid with high elasticity is slower than that of a Newtonian fluid. This is consistent with our experimental data, which show Bo > 1 for highly elastic fluids, indicating that more fluid is accumulated in the rim due to less destabilization. However, the quantification of the nonlinear effect of fluid elasticity on rim destabilization and its modeling remain unclear. The experimental critical value of $\tilde{\mathrm{De}}$ above which Bo = 1 breaks down is $\tilde{\mathrm{De}} \approx 16$ [Fig. 3(c)]. The theoretical explanation for this value is the subject of future research.

We showed that the rim destabilization during unsteady sheet fragmentation induces a self-adjustment of the instantaneous rim thickness b: it remains equal to the local instantaneous unsteady capillary length. Namely, the rim thickness is governed by a *local* and *instantaneous* Bond number $\mathrm{Bo} = \rho b^2(-\ddot{R})/\sigma = 1$. Such criterion is robust to a range of fragmentation geometries and to changes in fluid properties, including viscosity and elasticity. However, prerequisites need to be met to ensure that the Bo = 1 criterion shapes the rim thickness. First, the criterion only holds if sufficient fluid is contained in the rim. Second, initial perturbations need to be sufficient to trigger the unsteady instability ensuring growth of corrugations. This is illustrated in Fig. 4(a), showing the time evolution of the local rim Bo for drop impacts on smooth and rough surfaces. The former incurs less initial perturbations than the later, resulting in a longer time required for initial corrugations to grow into ligaments and, therefore, to reach Bo = 1. Third, the Bo = 1 criterion requires a sufficiently large acceleration and fluid influx into the rim. For instance, in the stationary case of a Savart sheet [43–45] the acceleration is null. Based on (4), the rim thickness would be infinite, clearly unrealistic. In this particular case the rim still destabilizes but its thickness is determined by the local geometry of cusps that develop around the rim [46].

For another unsteady sheet fragmentation process, drop impact on a deep pool leading to a crown splash, we find that the local Bond number of the rim remains smaller than 1 [Fig. 4(b)]. This is due to the important dissipation of impact kinetic energy via cavity formation below the surface, which decreases the fluid influx into the rim below what would be required to satisfy Bo = 1. The physical implication of Bo < 1 is that, contrary to impacts on thin films or surfaces, corrugations cannot grow. When observed, however, they appear to form at the very early stage of impact and are believed to originate from a different mechanism [31,47–50]. The complexity of the early stage of impact makes their origin difficult to elucidate. However, with the instantaneous local Bo < 1, no new ligaments emerge from the rim during its expansion. This is in contrast to the continuous emergence of new ligaments from unsteady rims from drop impacts on surfaces and thin films with Bo = 1 (Fig. 2). For drop impact on large solid surfaces, viscous stresses stabilize the rim: it accumulates fluid that cannot be shed; thus, the local Bo is systematically larger than 1 (Fig. 4b).

Beside unsteady expanding sheet fragmentation, fragmentation processes resulting from sheet rupture are also of interest. They arise, for example, from bursting bubbles [3] [Fig. 4(c)]. The sheet retraction on a bubble cap is governed by the constant Taylor-Culick retraction speed [51,52], yet

the curvature of the bubble cap induces a centripetal acceleration normal to the rim direction of motion. The rim thickness is first *primarily* driven by the scavenging of fluid throughout the hole opening, independent of the acceleration, leading to Bo < 1. Here, Bo is defined based on the constant initial centripetal acceleration. As fluid accumulates into the rim, eventually, the local instantaneous Bo reaches 1, coinciding with the growth of corrugations in the direction of the centripetal acceleration. Beyond that point, caution in interpretation of the later stage is required as the bubble cap sheet curves with a kink forming in the direction of the centripetal acceleration, in addition to no longer being a stretched film as the rest of the bubble collapses.

In the context of fluid fragmentation, our study represents a significant advance. Unsteady sheet fragmentation is ubiquitous in industrial and natural fluid processes, used for drug delivery [53], and important for transfer of biological and chemical compounds and pathogen spread. Prior studies neglected the role of unsteadiness on rim destabilization, in large part due to the lack of measurements enabling one to discriminate between hypotheses on the dominant instabilities taking place, but also due to the lack of a theoretical framework as tractable as that of steady classical hydrodynamic instabilities. We showed that a robust criterion of instantaneous local Bo $= 1$ governs the unsteady rim thickness. This criterion enables tremendous simplification of the modeling, and therefore the mechanistic understanding, of a large class of unsteady inviscid fragmentation processes. Moreover, we also showed for which fluid viscous and viscoelastic conditions the criterion continues to hold, thus allowing its application to a broader class of contaminated and non-Newtonian fluids important in biological processes such as violent exhalations or crop pathogen transport involved in disease transmission [4–7].

This research was supported in part by the USDA-NIFA Specialty Crop Research Initiative Grant Award No. MDW-2016-04938. Y. W. is grateful for the partial support of the MIT J. S. Hennessy OGE Fellowship. N. B. is grateful for the partial support of the National Science Foundation Graduate Fellowship. R. D. is grateful for the partial support of the MIT Dickson Fellowship, and S. P. is grateful for the support of the MIT Presidential Fellowship.

*lbouro@mit.edu

[1] A. L. Yarin, Drop impact dynamics: Splashing, spreading, receding, bouncing…, Annu. Rev. Fluid Mech. **38**, 159 (2006).

[2] A. Déchelette, E. Babinsky, and P. E. Sojka, Drop size distributions, in *Handbook of Atomization and Sprays: Theory and Applications*, edited by N. Ashgriz (Springer, Boston, MA, 2011), pp. 479.

[3] P. Walls, J. Bird, and L. Bourouiba, Moving with bubbles: A review of the interactions between bubbles and the microorganisms that surround them, Integrative and Comparative Biology **54**, 1014 (2014).

[4] L. Bourouiba, E. Dehandschoewercker, and J. W. M. Bush, Violent expiratory events: On coughing and sneezing, J. Fluid Mech. **745**, 537 (2014).

[5] B. E. Scharfman, A. H. Techet, J. W. M. Bush, and L. Bourouiba, Visualization of sneeze ejecta: Steps of fluid fragmentation leading to respiratory droplets, Exp. Fluids **57**, 24 (2016).

[6] L. Bourouiba and A. Sneeze, A Sneeze, N. Engl. J. Med. **375**, e15 (2016).

[7] T. Gilet and L. Bourouiba, Fluid fragmentation shapes rain-induced foliar disease transmission., J. R. Soc. Interface **12**, 20141092 (2015).

[8] E. Villermaux, Fragmentation, Annu. Rev. Fluid Mech. **39**, 419 (2007).

[9] J. Eggers and E. Villermaux, Physics of liquid jets, Rep. Prog. Phys. **71**, 036601 (2008).

[10] C. Clanet and E. Villermaux, Life of a smooth liquid sheet, J. Fluid Mech. **462**, 307 (2002).

[11] N. Bremond and E. Villermaux, Atomization by jet impact, J. Fluid Mech. **549**, 273 (2006).

[12] I. V. Roisman and C. Tropea, Impact of a drop onto a wetted wall: Description of crown formation and propagation, J. Fluid Mech. **472**, 373 (2002).

[13] C. Josserand and S. Zaleski, Droplet splashing on a thin liquid film, Phys. Fluids **15**, 1650 (2003).

[14] I. V. Roisman, T. Gambaryan-Roisman, O. Kyriopoulos, P. Stephan, and C. Tropea, Breakup and atomization of a stretching crown, Phys. Rev. E **76**, 026302 (2007).

[15] E. Berberović, N. P. van Hinsberg, S. Jakirlić, I. V. Roisman, and C. Tropea, Drop impact onto a liquid layer of finite thickness: Dynamics of the cavity evolution, Phys. Rev. E **79**, 036306 (2009).

[16] L. V. Zhang, J. Toole, K. Fezzaa, and R. D. Deegan, Splashing from drop impact into a deep pool: Multiplicity of jets and the failure of conventional scaling, J. Fluid Mech. **703**, 402 (2012).

[17] G. Agbaglah, M. J. Thoraval, S. T. Thoroddsen, L. V. Zhang, K. Fezzaa, and R. D. Deegan, Drop impact into a deep pool: Vortex shedding and jet formation, J. Fluid Mech. **764**, R1 (2015).

[18] I. V. Roisman, B. Prunet-Foch, C. Tropea, and M. Vignes-Adler, Multiple drop impact onto a dry solid substrate, J. Colloid Interface Sci. **256**, 396 (2002).

[19] Y. Wang and L. Bourouiba, Non-isolated drop impact on surfaces, J. Fluid Mech. **835**, 24 (2018).

[20] I. V. Roisman, K. Horvat, and C. Tropea, Spray impact: Rim transverse instability initiating fingering and splash, and description of a secondary spray, Phys. Fluids **18**, 102104 (2006).

[21] E. Villermaux and B. Bossa, Drop fragmentation on impact, J. Fluid Mech. **668**, 412 (2011).

[22] Y. Wang and L. Bourouiba, Drop impact on small surfaces: thickness and velocity profiles of the expanding sheet in the air, J. Fluid Mech. **814**, 510 (2017).

[23] A. L. Yarin and D. A. Weiss, Impact of drops on solid surfaces: Self-similar capillary waves, and splashing as a

new type of kinematic discontinuity, J. Fluid Mech. **283**, 141 (1995).
[24] C. Vernay, L. Ramos, and C. Ligoure, Free radially expanding liquid sheet in air: Time- and space-resolved measurement of the thickness field, J. Fluid Mech. **764**, 428 (2015).
[25] A. Rozhkov, B. Prunet-Foch, and M. Vignes-Adler, Impact of water drops on small targets, Phys. Fluids **14**, 3485 (2002).
[26] H. Lastakowski, F. Boyer, A. L. Biance, C. Pirat, and C. Ybert, Bridging local to global dynamics of drop impact onto solid substrates, J. Fluid Mech. **747**, 103 (2014).
[27] J. Eggers, M. A. Fontelos, C. Josserand, and S. Zaleski, Drop dynamics after impact on a solid wall: Theory and simulations, Phys. Fluids **22**, 062101 (2010).
[28] Y. Wang and L. Bourouiba, Unsteady sheet fragmentation: Droplet sizes and speeds (to be published).
[29] L. Rayleigh, On the instability of jets, Proc. R. Soc. Lond. A **s1-10**, 4 (1878).
[30] A. Rozhkov, B. Prunet-Foch, and M. Vignes-Adler, Dynamics of a liquid lamella resulting from the impact of a water drop on a small target, Proc. R. Soc. A **460**, 2681 (2004).
[31] L. V. Zhang, P. Brunet, J. Eggers, and R. D. Deegan, Wavelength selection in the crown splash, Phys. Fluids **22**, 122105 (2010).
[32] G. Taylor, The instability of liquid surfaces when accelerated in a direction perpendicular to their planes. I, Proc. R. Soc. A **201**, 192 (1950).
[33] I. R. Peters, D. van der Meer, and J. M. Gordillo, Splash wave and crown breakup after disc impact on a liquid surface, J. Fluid Mech. **724**, 553 (2013).
[34] R. Krechetnikov, Stability of liquid sheet edges, Phys. Fluids **22**, 092101 (2010).
[35] See Supplemental Material at http://link.aps.org/supplemental/10.1103/PhysRevLett.120.204503 for (i) The derivation of coupled Rayleigh-Taylor and Rayleigh-Plateau instability, (ii) The table summary of experiments conducted with information on fluid types and initial conditions; (iii) The time evolution of the radius of the expanding sheet.
[36] S. Chandrasekhar, *Hydrodynamic and Hydromagnetic Stability* (Clarendon Press, Oxford, England and Oxford University Press, New York, 1961).
[37] J. Eggers, Nonlinear dynamics and breakup of free-surface flows, Rev. Mod. Phys. **69**, 865 (1997).
[38] M. Goldin, J. Yerushalmi, R. Pfeffer, and R. Shinnar, Breakup of a laminar capillary jet of a viscoelastic fluid, J. Fluid Mech. **38**, 689 (1969).
[39] M. Gordon, J. Yerushalmi, and R. Shinnar, Instability of jets of non-Newtonian fluids, Trans. Soc. Rheol. **17**, 303 (1973).
[40] V. M. Entov and A. L. Yarin, Influence of elastic stresses on the capillary breakup of jets of dilute polymer solutions, Fluid Dyn. **19**, 21 (1984).
[41] A. L. Yarin, *Free Liquid Jets and Films: Hydrodynamics and Rheology*, Interaction of Mechanics and Mathematics Series (Longman Scientific & Technical, Harlow, Essex, 1993).
[42] G. H. Mckinley, Visco-elasto-capillary thinning and breakup of complex fluids, Annu. Rheo. Rev. **15**, 12 (2005).
[43] F. Savart, Mémoire sur le choc de deux veines liquides animées de mouvements directement opposés, Ann. Chim. **55**, 257 (1833).
[44] F. Savart, Mémoire sur le choc d'une veine liquide lancée sur un plan circulaire, Ann. Chim. **54**, 5687 (1833).
[45] F. Savart, Suite du mémoire sur le choc d'une veine liquide lancée sur un plan circulaire, Ann. Chim. **54**, 113145 (1833).
[46] J. M. Gordillo, H. Lhuissier, and E. Villermaux, On the cusps bordering liquid sheets, J. Fluid Mech. **754**, R1 (2014).
[47] R. D. Richtmyer, Taylor instability in shock acceleration of compressible fluids, Commun. Pure Appl. Math. **13**, 297 (1960).
[48] E. E. Meshkov, Instability of the interface of two gases accelerated by a shock wave, Fluid Dyn. **4**, 101 (1969).
[49] R. Krechetnikov and G. M. Homsy, Crown-forming instability phenomena in the drop splash problem, J. Colloid Interface Sci. **331**, 555 (2009).
[50] R. D. Deegan, P. Brunet, and J. Eggers, Complexities of splashing, Nonlinearity **21**, C1 (2008).
[51] G. I. Taylor, The dynamics of thin-sheets of fluid. I. water bells, Proc. R. Soc. A **253**, 289 (1959).
[52] F. E. C. Culick, Comments on a ruptured soap film, J. Appl. Phys. **31**, 1128 (1960).
[53] G. D. Porta, C. De Vittori, and E. Reverchon, Supercritical assisted atomization: A novel technology for microparticles preparation of an asthma-controlling drug, AAPS PharmSciTech **6**, E421 (2005).

SUPPLEMENTARY INFORMATION

Figure 1 shows a schematic diagram of a cylindrical liquid jet subjected to a body force in the direction perpendicular to the liquid jet. We consider the fluid inviscid and irrotational. The free surface of the jet is described by $y = f(t, x, z)$, or implicitly by $F(t, x, y, z) = y - f(t, x, z) = 0$. By introducing the velocity potential $\phi = \phi(t, x, y, z)$, the governing equations of the motion of the liquid jet reduce from Navier-Stokes equations to

$$\Delta\phi = 0$$
$$\frac{\partial\phi}{\partial t} + \frac{1}{2}|\nabla\phi|^2 = -\frac{1}{\rho}p - gy + C(t)$$

with $p = -\sigma\nabla\cdot\mathbf{n}$ and $\mathbf{n}$ is the outward normal unit vector of the jet free surface. The kinematic boundary condition at the free surface of the jet gives

$$\frac{DF}{Dt}(t, x, y, z) = 0 \quad \Longrightarrow \quad \frac{\partial F}{\partial t} + \nabla\phi\cdot\nabla F = 0$$

where $\Delta = \partial_x^2 + \partial_y^2 + \partial_z^2$ is the Laplacian operator. ρ, σ and p are the density, surface tension and pressure of the fluid, respectively. g is the body force exerted on the free jet, or an acceleration force in a non-inertial reference frame.

Considering the basic state of the jet with no perturbation and no motion ($\phi = 0$) and the free surface function $y = f_0(x, z)$, based on the static pressure balance at the free surface, we have the Young-Laplace equation

$$P_0 = -\rho g f_0 + \sigma\nabla\cdot\mathbf{n},$$

where P_0 can be considered as the external pressure distribution (ambient pressure). Thus, we can obtain

$$C(t) = -\frac{\sigma\nabla\cdot\mathbf{n}}{\rho} + gf_0 = -\frac{P_0}{\rho}$$

For a circular jet, the surface function f is expressed by introducing the cylindrical coordinate system as $r = f(t, \theta, x)$, namely, $F(t, r, \theta, x) = r - f(t, \theta, x) = 0$, with the outward normal vector $\tilde{\mathbf{n}}$ expressed as

$$\tilde{\mathbf{n}} = \nabla F(t, r, \theta, x) = \boldsymbol{i}_r - \frac{1}{r}\frac{\partial f}{\partial\theta}\boldsymbol{i}_\theta - \frac{\partial f}{\partial x}\boldsymbol{i}_x$$

where $\boldsymbol{i}_r$, $\boldsymbol{i}_\theta$ and $\boldsymbol{i}_x$ are the base vector for the cylindrical coordinates. For simplicity, we can denote the derivative of f with respect to θ and x by f_θ and f_x, respectively. Then, the unit outward normal unit vector $\mathbf{n}$ of the free surface is written as

$$\mathbf{n} = \frac{\tilde{\mathbf{n}}}{|\tilde{\mathbf{n}}|} = \frac{\boldsymbol{i}_r - \boldsymbol{i}_\theta f_\theta/r - \boldsymbol{i}_x f_x}{\sqrt{1 + f_\theta^2/r^2 + f_x^2}} \quad \text{at } r = f(t, \theta, x)$$

The total curvature $\nabla\cdot\mathbf{n}$ in cylindrical coordinates is expressed as

$$\nabla\cdot\mathbf{n} = \frac{1}{r}\frac{\partial}{\partial r}(rn_r) + \frac{1}{r}\frac{\partial n_\theta}{\partial\theta} + \frac{\partial n_x}{\partial x} \quad \text{at } r = f(t, \theta, x). \quad (1)$$

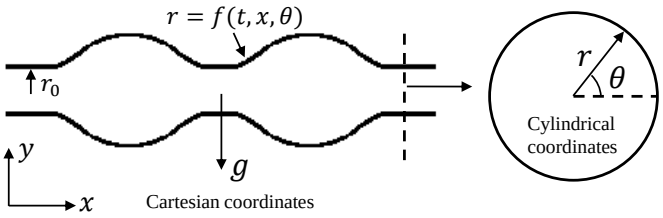

FIG. 1. Schematic diagram of a perturbed cylindrical liquid jet with its cross section

where n_r, n_θ and n_x represent the vector components of $\mathbf{n}$ in the three directions, rather than the derivatives.

To linearize the problem, we introducing a initial perturbation term in the free surface function by letting $f(t, \theta, x) = r_0 + f'(t, \theta, x)$, and assume the magnitude of the initial perturbation is much smaller than the jet radius, namely $|f'| \ll r_o$. By retaining the first-order term, the unit normal vector $\mathbf{n}$ and the total curvature $\nabla\cdot\mathbf{n}$ can be simplified as

$$\mathbf{n} \approx \tilde{\mathbf{n}} = \boldsymbol{i}_r - \frac{f_\theta}{r}\boldsymbol{i}_\theta - f_x\boldsymbol{i}_x$$
$$\nabla\cdot\mathbf{n} \approx \frac{1}{r}\frac{\partial}{\partial r}(r) - \frac{1}{r^2}f_{\theta\theta} - f_{xx} \approx \frac{1}{r_0} - \frac{f' + f'_{\theta\theta}}{r_0^2} - f'_{xx}$$

where $\mathbf{n}$, f and their derivatives are evaluated at the jet free surface $r = r_0 + f'$. Non-dimensionalizing the equation by choosing the characteristic lengthscale r_0 and capillary timescale $\tau_0 = \sqrt{\rho r_0^3/\sigma}$, the dimensionless variables are introduced to be

$$(\bar{\boldsymbol{x}}, \bar{f}) = \frac{1}{r_0}(\boldsymbol{x}, f), \quad \bar{t} = \frac{t}{\tau_0}, \quad \bar{\phi} = \frac{\tau_0\phi}{r_0^2}, \quad \bar{\nabla} = r_0\nabla$$
$$\bar{p} = \frac{\tau_0^2 p}{\rho r_0^2} = \frac{p}{\sigma/r_0}, \quad \bar{g} = \frac{\tau_0^2 g}{r_0} = \frac{\rho r_0^2 g}{\sigma} = \mathrm{Bo}.$$

To linearize, we write ϕ and p as $\phi(t, r, \theta, x) = \phi_0 + \phi'(t, r, \theta, x)$ and $p(t, \theta, x) = p_0 + p'(t, \theta, x)$. For the sake of simplicity, from now on, the hat symbol for dimensionless variables is omitted, unless noted otherwise. Thus, the linearized governing equation in dimensionless form gives the leading-order equation

$$p_0 = -1 \quad \text{and} \quad P_0 + \mathrm{Bo}\sin\theta = 1,$$

and the second-order equations:

$$\Delta\phi' = 0$$

with the boundary conditions at the free surface $r = 1$

$$\frac{\partial\phi'}{\partial t} = -p' - \mathrm{Bo}\, f'\sin\theta \qquad \text{and} \qquad \frac{\partial f'}{\partial t} = \frac{\partial\phi}{\partial r} \quad (2)$$

with $p' = f' + f'_{\theta\theta} + f'_{xx}$. Note that in this problem, the only governing equation is the Laplace Equation. The Euler equation after Lagrange-Cauchy integral becomes the boundary condition at the interface. To solve the

Laplace equation, we take the Fourier Transformation with respect to x, namely, letting

$$\hat{\phi}(k;t,r,\theta)=\int_{-\infty}^{+\infty}\phi'(t,r,\theta,x)e^{-ikx}\,\mathrm{d}x$$

Then, the Laplace equation becomes the Helmholtz equation (in cylindrical coordinates)

$$\frac{1}{r}\frac{\partial}{\partial r}\left(r\frac{\partial\hat{\phi}}{\partial r}\right)+\frac{1}{r^2}\frac{\partial^2\hat{\phi}}{\partial\theta^2}-k^2\hat{\phi}=0$$

Separating variable as $\hat{\phi}(k;t,r,\theta) = R(k;t,r)\Theta(t,\theta)$ yields two equations

$$\frac{\partial^2\Theta}{\partial\theta^2}+n^2\Theta=0$$
$$\xi^2\frac{\partial^2 R}{\partial\xi^2}+\rho\frac{\partial R}{\partial\xi}-(n^2+\xi^2)R=0$$

where n is an unknown coefficient to be determined and $\xi = kr$. The first equation can be easily solved by

$$\Theta(t,\theta)=A(t)\cos(n\theta)+B(t)\sin(n\theta)$$

Because of the cylindrical shape of the jet, $\Theta(t,\theta)$ has to satisfy the condition $\Theta(t,\theta)=\Theta(t,\theta+2\pi)$ for any time t, thus, n needs to be a integer. The second equation is the modified Bessel equation with the general solution as

$$R(\xi,t)=C(t)I_n(\xi)+D(t)K_n(\xi)$$

where I_n and K_n are the modified Bessel functions of first and second kinds with the order of n, respectively. However, K_n is unbounded at $\rho = 0$, which has to be eliminated by setting $D = 0$. The final solution of the second equation is

$$R(k;r,t)=C(t)I_n(kr)$$

Then, the final general solution of the Helmholtz equation can be expressed as

$$\hat{\phi}(k;t,r,\theta)=\sum_{n=0}^{\infty}\left(\phi_{kn}^{(c)}(t)\cos(n\theta)+\phi_{kn}^{(s)}(t)\sin(n\theta)\right)I_n(kr)$$

which yields the general solution of the Laplace equation

$$\phi(t,r,\theta,x)=\frac{1}{2\pi}\int_{-\infty}^{\infty}\hat{\phi}(k;t,r,\theta)e^{ikx}\,\mathrm{d}x$$

Here, since we only want to study the dispersion relation, our focus is on $\hat{\phi}(k;t,r,\theta)$, the solution of the Helmholtz equation in the frequency domain. Due to the linearity of the solution, $\phi_{kn}^{(c)}$ and $\phi_{kn}^{(s)}$ can be determined separately. In addition, based on the form of the solution, the surface perturbation function f' and the pressure perturbation function p' can be expressed as

$$p'(k;t,\theta)=\sum_{n=0}^{\infty}\left(p_{kn}^{(c)}(t)\cos(n\theta)+p_{kn}^{(s)}(t)\sin(n\theta)\right)$$
$$f'(k;t,\theta)=\sum_{n=0}^{\infty}\left(f_{kn}^{(c)}(t)\cos(n\theta)+f_{kn}^{(s)}(t)\sin(n\theta)\right)$$

To determine $\phi_{kn}^{(c)}$, putting the general solution into the boundary conditions (2) $r = 1$ and projecting onto the adjoint spectral space $\cos(m\theta)$ (multiplying by harmonics $\cos(m\theta)$ and integrating over $\theta\in[0,\pi]$) gives

$$I_n(k)\frac{d\phi_{kn}^{(c)}}{dt}\delta_{nn}^{(c)}=-p_{kn}\delta_{nn}^{(c)}-\mathrm{Bo}\sum_{m=0}^{\infty}\left(f_{km}^{(c)}\alpha_{mn}^{(cc)}+f_{km}^{(s)}\alpha_{mn}^{(sc)}\right)$$
$$\frac{\mathrm{d}f_{kn}^{(c)}}{\mathrm{d}t}=-kI_n'(k)\phi_{kn}^{(c)}\quad\text{and}\quad p_{kn}^{(c)}=(1-n^2-k^2)f_{kn}^{(c)}$$

where

$$\delta_{mn}^{(c)}=\int_0^{2\pi}\cos(m\theta)\cos(n\theta)\,\mathrm{d}\theta=\begin{cases}2\pi, & n=m=0\\ \pi, & n=m\geq 1\\ 0, & n\neq m\end{cases}$$

$$\alpha_{mn}^{(cc)}=\int_0^{2\pi}\cos(m\theta)\cos(n\theta)\sin(\theta)\,\mathrm{d}\theta=0$$

$$\alpha_{mn}^{(sc)}=\int_0^{2\pi}\cos(n\theta)\sin(m\theta)\sin(\theta)\,\mathrm{d}\theta$$
$$=\begin{cases}\pi & m=1,\ n=0\\ \pi/2 & m-n=1\ \&\ m\neq 1\\ -\pi/2 & n-m=1\ \&\ n\neq 1\\ 0 & \text{otherwise}\end{cases}$$

Combining the above equations gives

$$\frac{I_n(k)}{kI_n'(k)}\frac{d^2f_{kn}^{(c)}}{\mathrm{d}t^2}=(1-n^2-k^2)f_{kn}^{(c)}+\frac{\mathrm{Bo}}{\delta_{nn}^{(c)}}\sum_{m=0}^{\infty}\alpha_{mn}^{(sc)}f_{km}^{(s)}$$

To determine $f_{kn}^{(s)}$, similarly, projecting onto the adjoint spectral space $\sin(m\theta)$ gives

$$\frac{I_n(k)}{kI_n'(k)}\frac{d^2f_{kn}^{(s)}}{\mathrm{d}t^2}=(1-n^2-k^2)f_{kn}^{(s)}+\frac{\mathrm{Bo}}{\delta_{nn}^{(s)}}\sum_{m=0}^{\infty}\alpha_{mn}^{(cs)}f_{km}^{(c)}$$

where

$$\delta_{mn}^{(s)}=\int_0^{2\pi}\sin(m\theta)\sin(n\theta)\,\mathrm{d}\theta=\begin{cases}0, & n=m=0\\ \pi, & n=m\geq 1\\ 0, & n\neq m\end{cases}$$

$$\alpha_{mn}^{(ss)}=\int_0^{2\pi}\sin(m\theta)\sin(n\theta)\sin(\theta)\,\mathrm{d}\theta=0$$

$$\alpha_{mn}^{(cs)}=\int_0^{2\pi}\sin(n\theta)\cos(m\theta)\sin(\theta)\,\mathrm{d}\theta$$
$$=\begin{cases}\pi & n=1,\ m=0\\ \pi/2 & n-m=1\ \&\ n\neq 1\\ -\pi/2 & m-n=1\ \&\ m\neq 1\\ 0 & \text{otherwise}\end{cases}=\alpha_{nm}^{(sc)}$$

Due to the properties of the modified Bessel function, $I_n(x)' = I_{n+1}(x)$, so the equations are finally rearranged as

$$\frac{\mathrm{d}^2 f_{kn}^{(c)}}{\mathrm{d}t^2} = \frac{kI_{n+1}(k)}{I_n(k)}\left[(1-n^2-k^2)f_{kn}^{(c)} + \frac{\mathrm{Bo}}{\delta_{nn}^{(c)}}\sum_{m=0}^{\infty}\alpha_{mn}^{(sc)} f_{km}^{(s)}\right]$$
$$\frac{\mathrm{d}^2 f_{kn}^{(s)}}{\mathrm{d}t^2} = \frac{kI_{n+1}(k)}{I_n(k)}\left[(1-n^2-k^2)f_{kn}^{(s)} + \frac{\mathrm{Bo}}{\delta_{nn}^{(s)}}\sum_{m=0}^{\infty}\alpha_{mn}^{(cs)} f_{km}^{(c)}\right]$$

Based on our experiments, the perturbation is generally symmetric in the y-direction. Thus, $f_{kn}^{(c)}$ has nontrivial values only when n is even, and $f_{kn}^{(s)}$ does only when n is odd. For simplification of the solution, we truncate the equation to retain only the leading order term of $f_{k0}^{(c)}$ and $f_{k1}^{(s)}$. Thus, the governing equations reduce to:

$$\frac{\mathrm{d}^2 f_{k0}^{(c)}}{\mathrm{d}t^2} = \frac{kI_1(k)}{I_0(k)}\left[(1-k^2)f_{k0}^{(c)} + \frac{\mathrm{Bo}}{2}f_{k1}^{(s)}\right]$$
$$\frac{\mathrm{d}^2 f_{k1}^{(s)}}{\mathrm{d}t^2} = \frac{kI_2(k)}{I_1(k)}\left[(-k^2)f_{k1}^{(s)} + \mathrm{Bo} f_{k0}^{(c)}\right]$$

which can be written in matrix form

$$\frac{\mathrm{d}^2}{\mathrm{d}t^2}\begin{bmatrix} f_{k0}^{(c)} \\ f_{k1}^{(s)} \end{bmatrix} = \mathbf{A}\begin{bmatrix} f_{k0}^{(c)} \\ f_{k1}^{(s)} \end{bmatrix}$$
$$\text{with } \mathbf{A} = \begin{bmatrix} \frac{kI_1(k)}{I_0(k)}(1-k^2) & \frac{kI_1(k)\mathrm{Bo}}{2I_0(k)} \\ \frac{kI_2(k)\mathrm{Bo}}{I_1(k)} & \frac{kI_2(k)}{I_1(k)}(-k^2) \end{bmatrix}$$

Supposing $f_{k0}^{(c)} \sim e^{\omega t}\bar{f}_{k0}^{(c)}$ and $f_{k1}^{(s)} \sim e^{\omega t}\bar{f}_{k1}^{(s)}$, the dispersion relation of the equations gives

$$\det(\omega^{\mathbf{2}}\cdot\mathbf{I} - \mathbf{A}) = 0$$

$$\implies \quad \omega^4 + \left(\frac{kI_1(k)}{I_0(k)}(k^2-1) + \frac{kI_2(k)}{I_1(k)}k^2\right)\omega^2 + \frac{k^2 I_2(k)}{2I_0(k)}\left[2(k^2-1)k^2 - \mathrm{Bo}^2\right] = 0$$

The positive solution ω^2 of the equation is

$$\omega^2 = \frac{1}{2}\left(-\chi(k) + \sqrt{\chi(k)^2 - 4\psi(k)}\right)$$

$$\text{with} \quad \chi(k) = \frac{kI_1(k)}{I_0(k)}(k^2-1) + \frac{kI_2(k)}{I_1(k)}k^2$$
$$\text{and} \quad \psi(k) = \frac{k^2 I_2(k)}{2I_0(k)}\left[2(k^2-1)k^2 - \mathrm{Bo}^2\right]$$

which is the dispersion relation of the coupled Rayleigh-Plateau and Rayleigh-Taylor instability on a cylindrical liquid jet subjected to a body force in the radial direction. Here, the Bond number Bo is based on the radius of the liquid jet r_0. If based on the diameter (i.e. rim thickness $b = 2r_0$), there is a prefactor of 1/4 before Bo in the expression of $\psi(k)$.

TABLE I. Summary of the properties of the viscous and viscoelastic fluids used in the present study. Glycerol-water mixtures were used to vary the shear viscosity, μ. Mixtures of poly(ethylene oxide) (PEO, 1×10^6 g mol $^{-1}$) and poly(ethylene glycol) (PEG, 1×10^4 g mol $^{-1}$) with varying concentrations were used to obtain low values of relaxation times τ_E, and PEO solutions (4×10^6 g mol $^{-1}$) of varying concentrations were used to obtain higher values of τ_E. Here, the mixing percentage is with respect to the mass fraction of the compounds involved for PEO/PEG and to the volume fraction for glycerol. The shear viscosity values were measured using a shear-rheometer (TA instruments). The relaxation time for the PEO/PEG solutions was measured using an extensional rheometer (ThermoFisher Scientific) and that for the PEO solutions was referred from the literature [**?**]. Here, d_0, u_0, ρ, μ, and σ are the diameter, velocity, density, dynamic viscosity, and surface tension of the impacting drop, respectively. $\tau_{cap} = \sqrt{\rho d_0^3/8\sigma}$ is the capillary time characteristic of sheet expansion and fragmentation. We $= \rho u_0^2 d_0/\sigma$ is the Weber number, a measure of competition between inertial and surface tension effects. The Reynolds number Re $= \rho u_0 d_0/\mu$, the Ohnesorge number Oh $= \mu/\sqrt{\rho\sigma d_0}$, and the Deborah number De $= \tau_E/\tau_{cap}$ are measures of competition between inertial and viscous forces, viscous and surface tension effects, and elastic and surface tension effects, respectively. For all experiments, the impacting drop diameter is $d_0 = 4.3$ mm.

Fluid	ρ(kg/m^3)	σ(mN/m)	μ(mPa/s)	τ_E(ms)	τ_{cap}(ms)	Oh($\times 10^{-3}$)	De	u_0(m/s)	We($\times 10^2$)	Re($\times 10^3$)
Water	1.0	72	1.0	0	14	1.8	0	2.8	4.8	12
								3.4	6.9	15
								4.0	9.6	18
Glycerol(30%)	1.1	71	2.7	0	14	4.7	0	3.6	8.4	6.2
Glycerol(50%)	1.1	69	4.2	0	15	7.3	0	3.6	8.9	4.1
Glycerol(60%)	1.1	68	8.5	0	15	15	0	2.1	3.1	1.2
								3.4	8.6	2.0
Glycerol(68%)	1.2	66	14	0	15	24	0	3.5	9.3	1.3
								4.3	14	1.6
Glycerol(70%)	1.2	66	20	0	15	35	0	3.6	10	0.93
Glycerol(78%)	1.2	64	50	0	16	87	0	3.6	11	0.38
PEO(0.1%)-PEG(1%)	1.0	69	2.5	3.5	14	4.6	0.29	3.9	9.3	6.7
PEO(0.2%)-PEG(1%)	1.0	67	3.3	3.5	14	6.2	0.29	3.8	9.3	4.9
PEO(0.3%)-PEG(1%)	1.0	67	3.6	3.5	14	6.7	0.29	3.7	8.9	4.5
PEO(0.5%)-PEG(1%)	1.0	65	9.1	3.5	14	17	0.29	2.5	4.2	1.2
								3.7	9.1	1.7
								4.2	12	2.0
PEO(0.6%)-PEG(1%)	1.0	65	22	3.5	14	42	0.29	3.7	8.8	0.71
PEO(0.1%)	1.0	58	2.5	5.8	15	5.0	0.44	2.5	4.8	4.4
								3.7	10	6.3
								4.2	1.3	7.3
PEO(0.25%)	1.0	58	9.1	16	15	18	1.2	2.5	4.7	1.2
								3.7	9.9	1.7

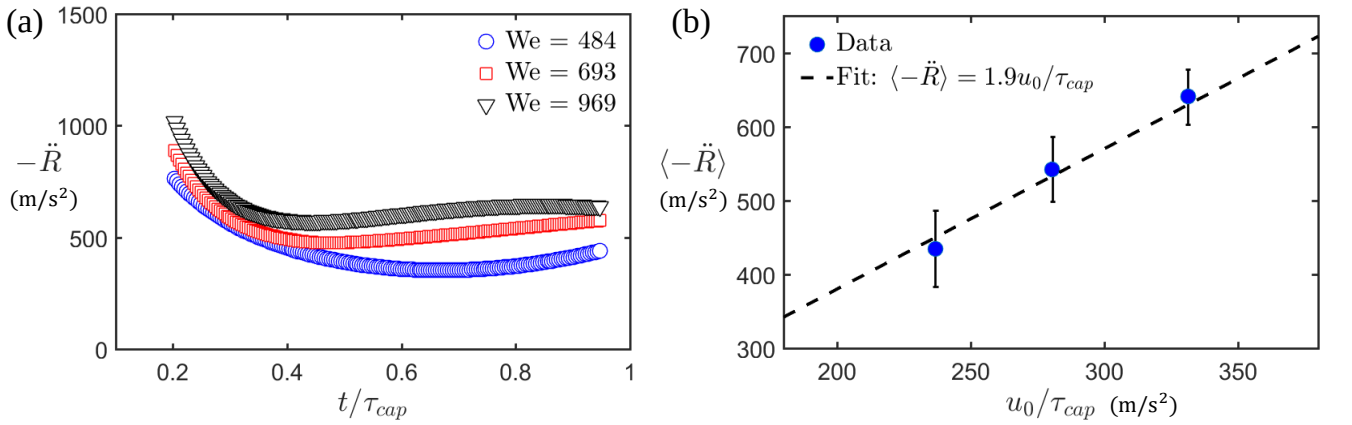

FIG. 2. (a) Time evolution of the sheet acceleration during its expansion. (b) The relation of mean acceleration $\langle -\ddot{R} \rangle$ follows the scale of u_0/τ_{cap} with a prefactor around 1.9. Namely, $\langle -\ddot{R} \rangle = 1.9 u_0/\tau_{cap}$.